J. Fluid Mech. (2010), *vol.* 647, *pp.* 391–402.
doi:10.1017/S0022112010000091

Experimental study of flow fields in an airway closure model

S. BIAN[1]†, C.-F. TAI[1], D. HALPERN[2], Y. ZHENG[1] AND J. B. GROTBERG[1]

[1]Department of Biomedical Engineering, University of Michigan, Ann Arbor, MI 48109, USA

[2]Department of Mathematics, University of Alabama, Tuscaloosa, AL 35487, USA

(Received 25 September 2009; revised 18 December 2009; accepted 28 December 2009)

The liquid lining in small human airways can become unstable and form liquid plugs that close off the airways. Bench-top experiments have been performed in a glass capillary tube as a model airway to study the airway instability and the flow-induced stresses on the airway walls. A microscale particle image velocimetry system is used to visualize quantitatively the flow fields during the dynamic process of airway closure. An annular film is formed by injecting low-viscosity Si-oil into the glycerol-filled capillary tube. The viscosity ratio between these two fluids is similar to that between water and air. The thickness of the film varies with the infusion rate of the core fluid, which is controlled by a syringe pump. After a uniform film is formed, the syringe pump is shut off so that the core flow speed is close to zero during closure. Instantaneous velocity fields in the annular film at various stages of airway closure are computed from the images and analysed. The wall shear stress at the instant when a liquid plug forms is found to be approximately one order of magnitude higher than the exponential growth period before closure. Within the short time span of the closure process, there are large wall shear stress fluctuations. Furthermore, dramatic velocity changes in the film flow during closure indicate a steep normal stress gradient on the airway wall. The experimental results show that the wall shear stress during closure can be high enough to injure airway epithelial cells. An airway that experiences closure and reopening cyclically during breathing could be injured from fluid forces during both phases of the cycle (i.e. inspiration and expiration).

1. Introduction

The lung's airways are coated with an annular liquid film. It is well known that when the disturbance in the liquid lining is amplified, a plug can be formed that closes off the airway. In normal gravity, closure usually occurs in the lower airway of an upright human. In a microgravity environment, airway closure tends to be more homogeneous and might be found in the upper airways. The formation of a liquid plug might limit the gas exchange if the closing volume is large. Furthermore, the formation of this plug can lead to the complete collapse of the airway due to the axial draining of ambient film fluid into the plug (Macklem, Proctor & Hogg 1970; Greaves, Hildebrandt & Hoppin 1986). Airway closure usually happens in the small airways near the end of expiration, and is often accompanied with hypersecretion or/and surfactant deficiency in the airway in a variety of lung diseases, such as

† Email address for correspondence: sbian@umich.edu

chronic obstructive pulmonary disease (COPD; Guerin *et al.* 1997), cystic fibrosis (Griese *et al.* 2004), acute respiratory distress syndrome (ARDS; Baker *et al.* 1999), pneumonia (Gunther *et al.* 1996), bronchiolitis (Dargaville, South & McDougall 1996) and asthma (t Veen *et al.* 2000). When the airway is inflated during inhalation, the plug might rupture and the airway reopens. The transient pressure wave generated by the abrupt reopening might be detected by a stethoscope as a crackle sound (Piirila & Sovijarvi 1995).

Modelling work by Halpern & Grotberg (1992) has shown that several forces could contribute to airway closure, such as surface tension instability and wall compliance. Experiments in a capillary tube were conducted by Cassidy *et al.* (1999) to examine the effects of surfactant on airway closure. They measured the relationship between the film thickness at various infusion flow rate of the core fluid, the instability growth rate and the closure time. It was found that the surfactant decreased the growth rate by 20 % and increased the closure time as well as the critical film thickness. A review of the mechanics of airway closure is given by Heil, Hazel & Smith (2008) and includes a description of both the purely fluid-mechanical 'film collapse' and the coupled, fluid-elastic 'compliant collapse' mechanism.

Flow-induced stresses on the airway epithelia might lead to severe cell injury. Gaver and colleagues (Bilek, Dee & Gaver 2003; Kay *et al.* 2004) experimentally investigated cell injury during airway reopening by using semi-infinite air bubbles moving through a parallel-plate chamber lined with cultured pulmonary epithelial cells. Significant cell damage was found because of the mechanical stress induced by the bubble propagation. It was also revealed that pulmonary surfactant relieves the flow-induced stresses and, consequently, decreases cell damage. Experimental studies (Muscedere *et al.* 1994; Taskar *et al.* 1997) on excised lungs and *in vivo* animal models have shown that severe tissue damage was found in surfactant-deficient lungs because of the repetitive airway reopening. Ghadiali & Gaver (2008) gave a review of the effects of surface tension forces on the mechanics of airway reopening and epithelial cell injury. Huh *et al.* (2007) illustrated that exposure of primary human airway epithelial cells to plug propagation and rupture led to significant cell injury. Numerical simulations of liquid plug propagation in a rigid channel (Fujioka & Grotberg 2004, 2005; Fujioka, Takayama & Grotberg 2008) confirmed that sharp peaks in wall stresses and stress gradients were present in the transition region of the plug during the propagation. In addition, experimental and numerical studies of plug propagation in flexible microchannels (Zheng *et al.* 2009) predicted a higher level of wall stresses and stress gradients along the highly deformable wall as compared to a rigid channel wall.

Although it is well recognized that airway reopening can induce epithelial damage from fluid forces, it has not been appreciated that airway closure may also be injurious. Dramatic changes in the flow velocity and pressure in the film fluid during the dynamic process of airway closure can lead to high stress and stress gradients that might damage the epithelial cells on the airway. Although the growth of the capillary instability in the liquid lining of a rigid tube was thoroughly measured and simulated by Cassidy *et al.* (1999), the velocity field in the film fluid has not been experimentally measured. Quantifying the velocity field is critical to understanding the flow-induced stresses on the airway epithelial cells during airway closure and, therefore, is of great importance in sustaining the normal functions of the lung and preventing deleterious fluid-induced stresses.

In the current bench-top experiments described in § 2, we use a rigid capillary tube as a small airway model and study the flow during the dynamic process of the airway

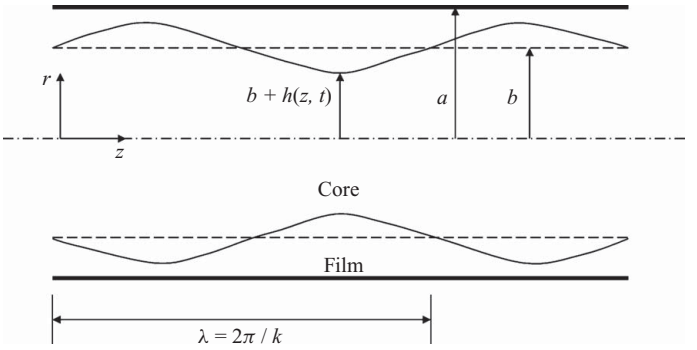

FIGURE 1. Schematic of the unstable liquid film lining a capillary tube with circular cross-section. a is the inner radius of the rigid tube, b is the radius of the undisturbed core fluid, h is the amplitude of the film disturbance and λ is the wavelength of the disturbance.

closure. A viscous glycerol film is formed by injecting a less viscous Si-oil into the glycerol-filled tube uniformly seeded with fluorescent particles. The dynamic viscosity ratio between the film and the core fluid is close to that between water and air. The effective Reynolds numbers for both the film and the core fluids are physiologically realistic when compared with those in the lung system. Gravitational effects are negligible as the density difference between the two fluids is small. Microscale particle image velocimetry (micro-PIV) measurements are conducted to quantitatively measure the velocity fields in the film fluid as the disturbance grows with time until a liquid plug is formed. The initial film thickness, which is a function of the infusion speed of the core fluid, is compared with previous results (Fairbrother & Stubbs 1935; Bretherton 1961; Halpern, Jensen & Grotberg 1998). We examine the velocity fields in the film fluid before and after the closure as well as the stress distributions.

2. Experimental set-up

2.1. *Test parameters*

The schematic of a capillary tube with circular cross-section lined with unstable liquid film is given in figure 1. An important dimensionless parameter is $\varepsilon = (a-b)/a$, where $(a-b)$ is the undisturbed film thickness and a is the inner radius of the rigid tube. In normal lung airways, the dimensionless film thickness ε is very thin, ranging from 0.02 to 0.04. However, hyper-secretion or fluid accumulation is commonly found in patients' airways with lung diseases such as COPD and ARDS and asthmatic lungs have decreased airway diameters, which leads to higher ε values in unhealthy lungs. Gauglitz & Radke (1988) determined that the minimum film thickness for the closure, ε_{crit}, was approximately 0.12 based on their lubrication theory models and obtained an average of $\varepsilon_{crit} = 0.09$ from their experimental results. When ε is smaller than ε_{crit}, the disturbance waves may grow to form periodic collars throughout the tube without occluding it. Everett & Haynes (1972) found that the collar volume within one axial wavelength needs to exceed $5.47a^3$ in order to form a plug. Kamm & Schroter (1989) obtained similar results by dripping oil into small vertical rigid tubes. Furthermore, Halpern & Grotberg (1993) found that ε_{crit} increases if surfactant exists in the system. In the current study, the dimensionless thickness of the undisturbed film is in the range of 0.10–0.32 for the micro-PIV measurements and the surface tension is assumed to be constant in our experimental system. The Capillary number

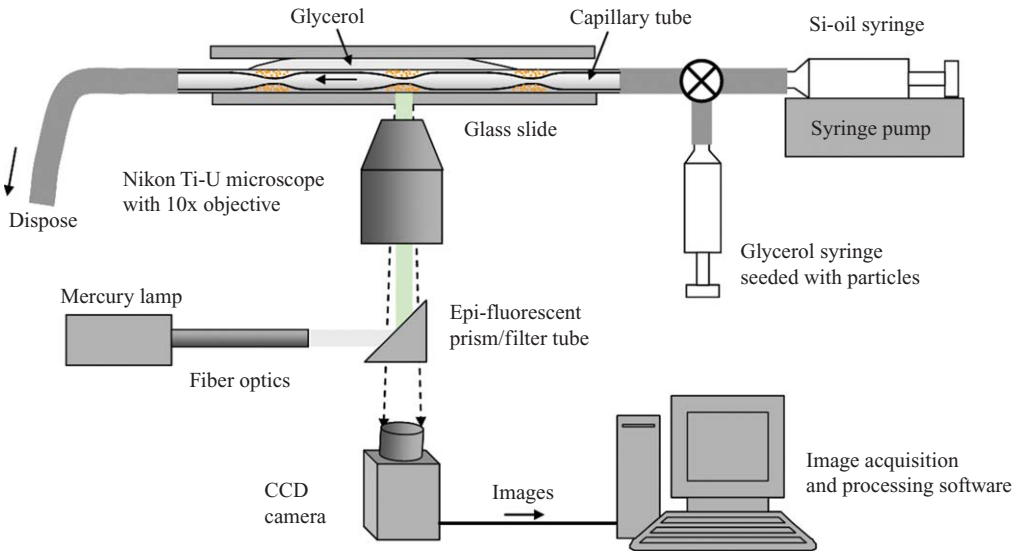

FIGURE 2. Schematic of the experimental apparatus for micro-PIV measurements.

for the film formation is defined as $Ca = \mu_{film} U^*/\sigma^*$, where μ_{film} is the film viscosity, σ^* is the interfacial surface tension between the two fluids and U^* is the average infusion speed of the core fluid. In this study, Ca is in the range of 0.024–0.47.

High viscosity 96 % glycerol is used as the film fluid and the low-viscosity Si-oil as the core fluid. The dynamic viscosity ratio is approximately 100:1, close to that between water and air. The interfacial tension between these two fluids is approximately 30 dyn cm^{-1}, measured by a stand-alone tensiometer (K8, Kruss), which is close to 31 dyn cm^{-1} of the tracheal surface tension measured in normal horse lungs (Hof *et al.* 1997), or 33 and 32 dyn cm^{-1} (Lee *et al.* 1995) in normal rat and guinea pig lungs, respectively. The surface tension in normal human pulmonary airways is approximately 20–25 dyn cm^{-1} (Goerke & Clements 1986; Green *et al.* 1991).

The Bond number, $Bo = (\rho_{film} - \rho_{core}) g a^2/\sigma^*$, represents the ratio of gravitational to surface tension effects. In our experiments, gravitational effects are negligible since a liquid–liquid system with similar densities between the liquids is used. The effective Bond number $\varepsilon^{-1} Bo = 0.04 \sim 0.1 = 1$ in the current airway model, which is consistent with the magnitude of Bond numbers found in small airways (Hammond 1983). Inertia in the film layer can be neglected provided that the effective Reynolds number for the liquid film, $\varepsilon^2 Re = (\varepsilon^5 \rho_{film} \sigma^* a)/\mu_{film}^2 = 1$, which holds in the lungs (Cassidy *et al.* 1999).

2.2. *Film generating system*

The experimental apparatus is shown schematically in figure 2. A rigid, thin borosilicate glass capillary tube with an inner diameter of 580 μm is chosen as the airway model, which is close to 490 μm, the mean airway diameter at generation 16 in normal human lungs. The length of the capillary is trimmed to be approximately 20 cm. The capillary tube is immersed in glycerol and held between two glass slides to eliminate visual distortion. Both the borosilicate glass and the glycerol have a refraction index of 1.473. Before the test, the high-viscosity glycerol is manually injected into the capillary tube using a 5 ml syringe via the three-way valve. The direction of the valve is then switched so that the path for feeding the glycerol is

cutoff allowing for the injection of the core fluid. Depending on the desired film thickness, a syringe pump (PHD 2000, Harvard Apparatus) with a pre-set infusion rate drives the Si-oil through the glycerol-filled capillary tube. The core flow is stopped once the film is formed uniformly throughout the tube. The average core fluid velocity is defined as the infusion flow rate divided by the cross-sectional area of the core. In the current study, the flow infusion rate of the syringe pump ranges from 1 μl min^{-1} to 300 μl min^{-1}, resulting in an undisturbed film thickness ε ranging from 0.1 to 0.32, which is measured at several locations after the uniform film is formed and before the disturbance is visible. The interface between the film and the core fluids is then closely monitored for the growth of the small waves. Complete details of the film formation and the wave development are given by Cassidy *et al.* (1999).

2.3. *Micro-PIV system*

A Nikon inverted microscope (Nikon Eclipse Ti-U, Nikon Co.) is used to view the capillary tube at 10× magnification. A 12 bit CCD camera (Photometric Coolsnap EZ) with 1392 × 1040 pixels resolution is attached to the side of the microscope for observing the area of interest and acquiring the images. The field of view (FOV) is 905 × 676 μm, which leads to a spatial resolution of 0.650 μm $pixel^{-1}$ in our experiments. The film fluid glycerol is uniformly seeded with 1 μm diameter fluorescent particles (Nile Red, FluoSpheres, Invitrogen Co.) before being injected into the capillary. The particles have excitation/emission peaks at 535/575 nm. The volumetric illumination for the micro-PIV measurements is provided by a metal halide illumination system (X-cite 120, EXFO). The light beam is guided through an optical fibre into the microscope, where the beam is first refracted and redirected by an epi-fluorescent prism and then filtered by the built-in fluorescence filter to get the light of desired wavelength. The camera captures the emitted light from the excited fluorescent particles and stores the particle images in the computer RAM after being triggered by the image acquisition software (MetaMorph, Universal Imaging Co.).

The time interval between two particles images is determined by the camera frame rate and exposure time. In the current study, the camera frame rate is approximately 10 frames s^{-1} at the full viewing capacity, which means that the time interval between two frames is approximately 0.1 s. Davis 7.1 software (Lavision Inc.) is used to process the particle images and compute the vector fields using an fast Fourier transform (FFT) cross-correlation algorithm with the multi-pass iteration method. The final computation window size is 32 × 32 pixels with 50 % overlap, resulting in a vector spacing of 10.4 μm. Consequently, there are approximately 3–6 vectors in the liquid film before the wave amplifies and 87 vectors in the axial direction. Experimental results are given in § 4.

3. Results and discussions

3.1. *Initial film thickness*

It is well known that the film thickness depends on the Capillary number (Cassidy *et al.* 1999). We chose eight different infusion speeds from 0.095 to 1.89 cm s^{-1}, and, for each speed, the experiment was repeated four or five times to obtain a statistical mean film thickness. The film thickness at different infusion speeds was measured under bright-field illumination, separately from the micro-PIV experiments. Previous studies (Fairbrother & Stubbs 1935; Taylor 1961; Goldsmith & Mason 1963) provide an empirical equation for ε for $10^{-4} < Ca < 10^{-1}$

$$\varepsilon = 0.5(Ca)^{1/2}. \tag{1}$$

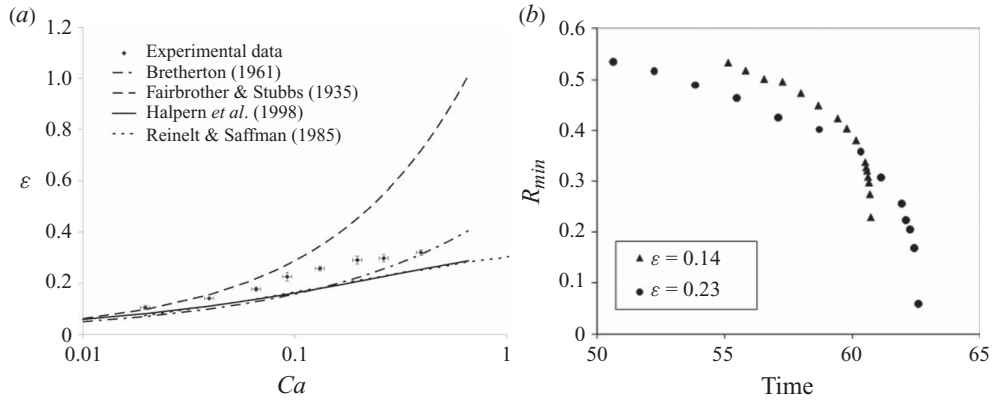

FIGURE 3. (*a*) $\varepsilon = (a - b)/a$ versus Capillary number $Ca = \mu_{film}U^*/\sigma^*$ of the film fluid. (*b*) The change of core radius ratio with time. The non-dimensional time is scaled as $t = t^*/(a\mu_{film}/\varepsilon^3\sigma^*)$.

For $10^{-4} < Ca < 10^{-2}$, Bretherton's (1961) theoretical analysis suggests that

$$\varepsilon = 0.643(3Ca)^{2/3}. \tag{2}$$

Reinelt & Saffman (1985) studied the penetration of a finger into a viscous fluid by using Stokes equations for a low-Reynolds-number flow. They computed the relationship between the film thickness and the Capillary number for both the two-dimensional and axisymmetric cases. Halpern *et al.* (1998) developed a formula for the trailing film thickness of a liquid plug propagating in a tube with circular cross-section

$$\varepsilon = 0.36\{1 - \exp(-2Ca^{0.523})\}. \tag{3}$$

Figure 3(*a*) shows the undisturbed film thickness, ε, versus the Capillary number for the film formation, Ca, in the current experiments compared with previous studies. The film thickness increases with Ca. For $Ca \ll 1$, the film thickness is in good agreement with the theoretical predictions by Bretherton (1961), Reinelt & Saffman (1985) and Halpern *et al.* (Halpern & Gaver 1994; Halpern *et al.* 1998). As Ca approaches $O(1)$, the measured data support the analysis by Reinelt & Saffman (1985) and Halpern *et al.* (Halpern & Gaver 1994; Halpern *et al.* 1998).

3.2. *The disturbance growth*

The growth rate of the disturbance q^* is found to be dependent on the non-dimensional wavenumber K (Rayleigh 1892; Cassidy *et al.* 1999), where $K = k^*b = 2\pi b/\lambda^*$, k^* is the dimensional wavenumber and λ^* is the wavelength of the disturbance. In the experiments, the non-dimensional wavenumber, K, is approximately equal to 0.68. This value is in good agreement with the instability analysis for a cylindrical jet by Rayleigh (Rayleigh 1892), where the critical disturbance wavenumber K_{crit} for the maximum growth rate is found to be $K_{crit} = \pi/4.5$, with $K = k^*b = 2\pi/\lambda$.

The closure time is determined in the same fashion as it was done by Cassidy *et al.* (1999). Because the disturbance begins to grow before the magnitude is detectable visually, it is important to estimate the start time of the disturbance from the growth rate of the disturbance. This is done by assuming that the disturbance initially grows exponentially. A normal mode expression for the dimensionless disturbance amplitude $h = h*/\varepsilon a$ can be written as

$$h = h_1 e^{q^*t^* + ik^*z^*}. \tag{4}$$

By plotting $\ln h$ versus t^* and curve fitting the data linearly, the start time t_0^* can be determined to be the time at which the fitted line intercepts with $h = h_1$, where the initial amplitude h_1 is set to be 5 % of the undisturbed film thickness ε. The determination of the non-dimensional closure time t_{c1} for different ε was given in detail by Cassidy *et al.* (1999), where

$$t_{c1} = \frac{t_c^*}{a\mu_{film}/\sigma^*}. \tag{5}$$

In the experiments, the closure time t_c^* is found to be approximately 37.4 s for $\varepsilon = 0.23$ and 160.5 s for $\varepsilon = 0.14$, leading to $t_{c1} = 5158$ and 22135, respectively. These non-dimensional closure times are in good agreement with previous experimental and theoretical values acquired by Cassidy *et al.* (1999).

Figure 3(*b*) shows the change of the minimum radius of the interface R_{min} versus time for two different ε. For both ε, the disturbance grows exponentially and then accelerates when the time approaches the closure time. For smaller ε, the acceleration is faster, indicated by larger R_{min} during the exponential growth period. The non-dimensional closure time t_c, scaled by $a\mu_{film}/\varepsilon^3\sigma$, is 60.7 and 62.8 for $\varepsilon = 0.14$ and 0.23, respectively, showing a good agreement between the experimental closure times using the above-mentioned scaling method.

3.3. *Flow fields*

Time sequences of sample micro-PIV images before closure are given in figure 4(*a*). Instantaneous velocity vectors, speed contours and streamlines at two different times before the closure are shown in figure 4(*b*), which are derived from the three particle images in figure 4(*a*) using the PIV computing process described in § 2.3. The streamline plots indicate that the liquid is driven from the end of the film domain towards the centre. This is due to the capillary instability that induces a pressure gradient within the liquid layer and the conservation of volume within the layer. The velocity maximum is located at the bulge tip and a second velocity peak is found locally at the transition regions between the film and the bulge. The velocity at the tip accelerates as t approaches t_c, which is consistent with the acceleration of the disturbance growth rate. The streamlines are approximately perpendicular to the free surface of the tip area, while a vortical structure is observed near the free surface between the tip and the transition areas, consistent with the numerical results obtained by Campana, Di Paolo & Saita (2004).

Figure 5 shows the time sequences of the particle images from the micro-PIV measurements and the corresponding velocity fields after closure. After the formation of the plug, the fluid is continuously drained into the plug from the film region and the plug length extends along the axial direction, which might further induce the complete collapse of airways with compliant walls (Macklem *et al.* 1970; Greaves *et al.* 1986). The magnitude of the velocity at the interface decelerates as time increases beyond the closure time.

3.4. *Wall shear stresses*

In the experiment, the wall shear stress is computed by determining the radial gradient of the axial velocity gradient at the wall using two data points. Using three data points and polynomial curve-fitting method has been proved to yield similar results. Figure 6(*a*) shows the wall shear stresses acquired from the experimental data along the longitudinal axis for various time values. It can be seen that the location of the maximum wall shear stress moves towards the bulge ($z = 0$) as $t \to t_c$, which is consistent with the presence of the local velocity peaks seen in figure 4(*b*).

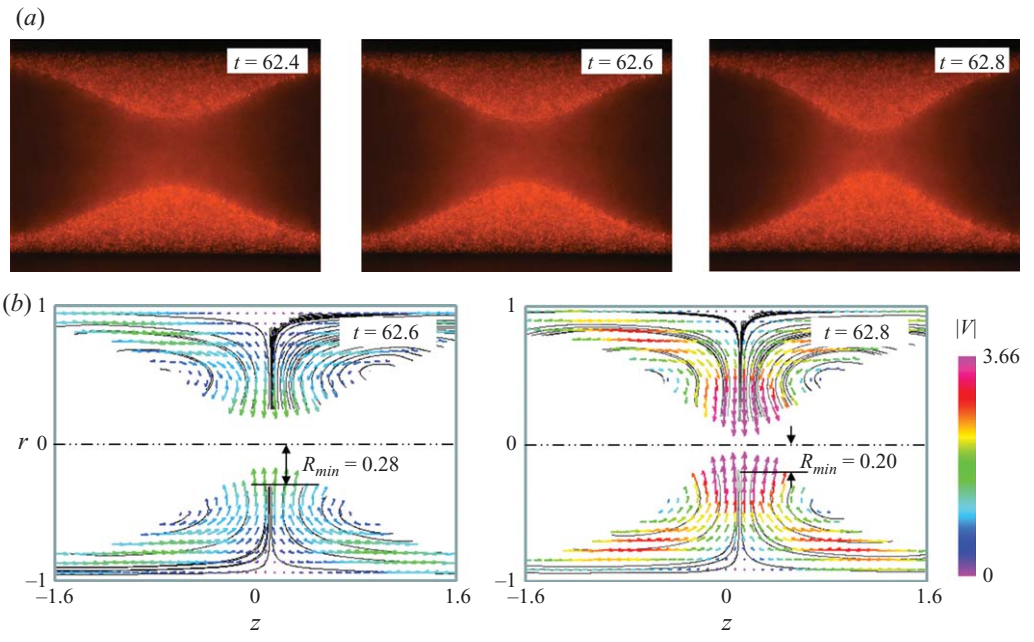

FIGURE 4. (*a*) Time sequences of micro-PIV images before the closure; (*b*) velocity fields, speed contours and streamlines in the film flow after the closure derived from micro-PIV images. The undisturbed film thickness $\varepsilon = 0.23$. The non-dimensional time is scaled as $t = t^*/(a\mu_{film}/\varepsilon^3\sigma^*)$ and the non-dimensional speed is scaled by $\varepsilon^3\sigma^*/\mu_{film}$. Only one-fourth of the vectors are presented here for the sake of clarification.

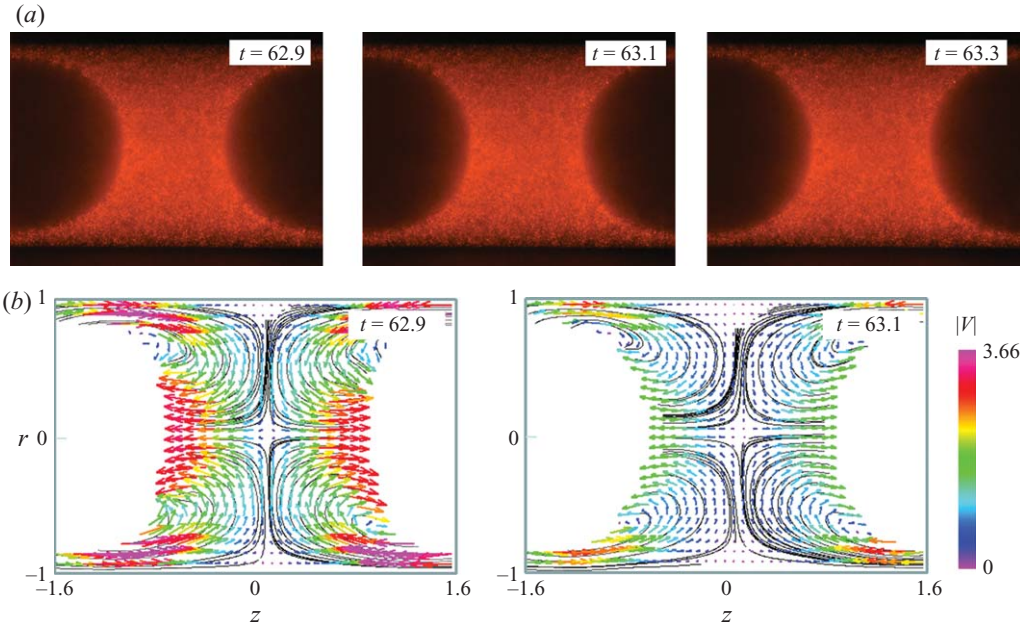

FIGURE 5. (*a*) Time sequences of micro-PIV images after the closure; (*b*) velocity fields, speed contours and streamlines in the film flow after the closure derived from micro-PIV images. The undisturbed film thickness $\varepsilon = 0.23$. The time is scaled by $t = t^*/(a\mu_{film}/\varepsilon^3\sigma^*)$ and the non-dimensional speed is scaled by $\varepsilon^3\sigma^*/\mu_{film}$. Only one-fourth of the vectors are presented here for the sake of clarification.

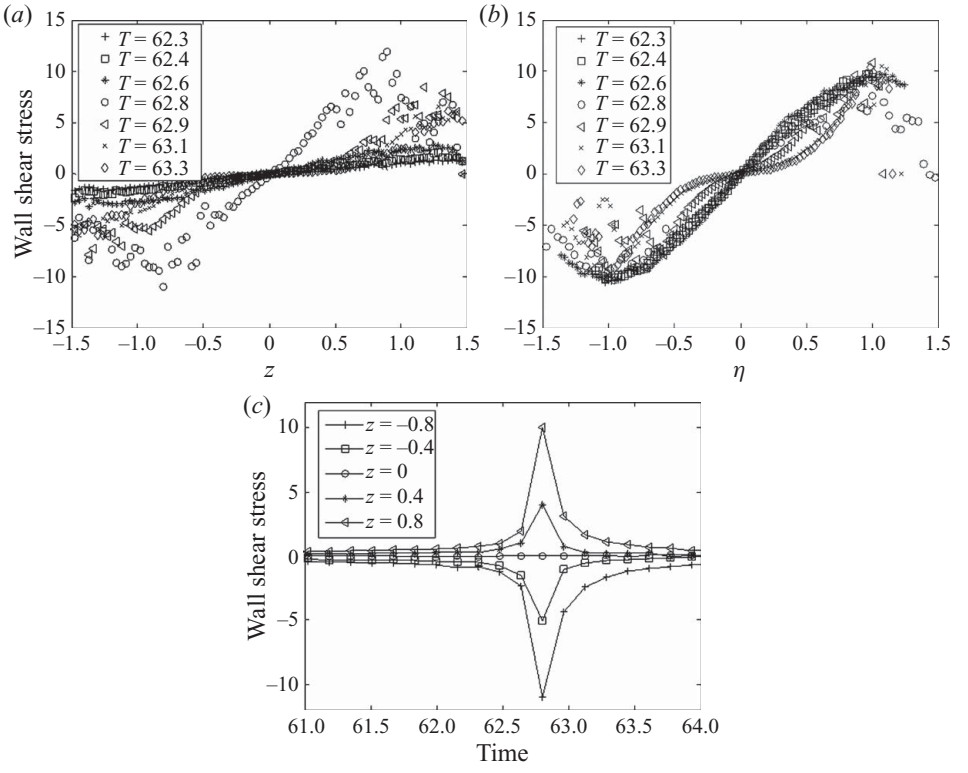

FIGURE 6. (*a*) The profiles of the non-dimensional wall shear stress along the longitudinal axis at various times before and after the closure. The stress scale is $\varepsilon^3\sigma^*/a$; (*b*) the profiles of wall shear stress scaled by the maximum wall shear stress at the local time; (*c*) time history of the wall shear stress at various longitudinal locations. The closure time t_c is approximately 62.8 and the undisturbed film thickness $\varepsilon = 0.23$.

In figure 6(*b*), the wall shear stress is scaled by the maximum wall stress value at each measured time. The non-dimensional parameter η is defined as z/z_{max}, where z_{max} is the axial location of the maximum wall shear stress. It can be seen that nearly all of the wall shear stress data collapse into one single sinusoidal curve before closure, indicating that the film growth is dominated by linear instability until the very last instant when the evolution of the film starts to be affected by nonlinear effects. After closure, the distribution of the wall shear stress drifts away from the collapsed curve. However, it is noteworthy that the wall shear stress evolves into another curve two time frames after closure, when the plug length extends gradually along the axial direction.

The evolution of the wall shear stress versus time at various longitudinal locations is shown in figure 6(*c*). The results indicate that the wall shear stress increases gradually and then accelerates rapidly when closure is about to occur. The magnitude of the wall shear stress near $t = t_c$ becomes approximately 1 order of magnitude higher than that during the exponential growth period of the disturbance, which is approximately 80 % of t_c. The closure time is clearly marked by the sharp peak of the wall shear stress at all locations.

Similar profiles of the wall shear stress are observed in figure 7 for $\varepsilon = 0.14$. The wall shear stress increases and the location of the maximum wall shear stress

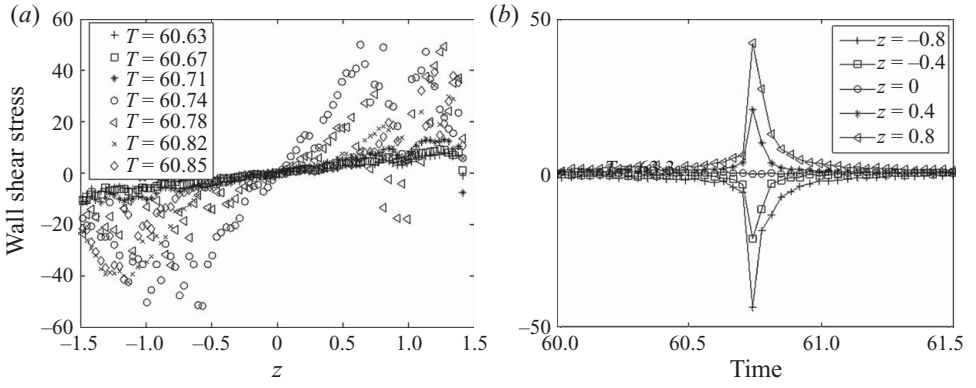

FIGURE 7. The profiles of the non-dimensional wall shear stress for $\varepsilon = 0.14$, scaled by $\varepsilon^3\sigma^*/a$: (*a*) the wall shear stress along the longitudinal axis at various time before and after the closure; (*b*) time history of the wall shear stress at various longitudinal locations, with $R_{min} = 0.25$ at the peak point.

shifts towards the centre of the bulge as $t \to t_c$. The time history shows that the wall shear stress increases and then accelerates rapidly as $t \to t_c$, and the closure time t_c is marked by the sharp peak at all locations. It is noteworthy that the non-dimensional wall stress for $\varepsilon = 0.14$ is almost 5 times higher than that for $\varepsilon = 0.23$, which might be due to the presence of ε^3 in the scaling leading to a factor of 4.4 between the characteristic stress/pressure values. It indicates the dimensional wall shear stress values are independent of ε. However, the temporal resolution of the PIV measurements is limited at 0.1 s, while the velocity and the shear stress change rapidly in the final acceleration stage of airway closure. A slight shift in time can cause a dramatic change in the stress value. Therefore, the dependence of the wall shear stress on ε is to be further investigated.

Experimental measurements in the model airway confirm that as $t \to t_c$, the wall shear stress increases significantly. During airway closure, epithelial cells experience not only a high shear stress but also a spatial gradient and a dramatic temporal fluctuation, which might be injurious to the cells.

4. Concluding remarks

The liquid lining in small human airways is unstable and can form liquid plugs that close off the airways. Bench-top experiments have been performed in a glass capillary tube as a model airway to study the airway instability and the flow-induced stresses on the airway walls.

Micro-PIV measurements have been used to obtain the flow fields during the dynamic process of liquid plug formation in a capillary tube. Instantaneous velocity fields in the annular film at various stages of airway closure show multiple local velocity peaks located at the bulge tip and the transition region. The velocity magnitude during closure is found to be approximately one order of magnitude higher than that during the exponential growth period of the disturbance before closure and that during the deceleration of the plug expanding period after closure. The wall shear stress at the time instant of closure is one order of magnitude larger than that before and after closure, indicating a large shear stress spatial gradient and temporal gradient on the airway wall, which might cause severe cell damage.

We thank Dr Benjamin Vaughan and Dr Marcel Filoche for their insightful comments on this manuscript. This work is supported by NIH grants HL85156 and HL84370.

REFERENCES

Baker, C. S., Evans, T. W., Randle, B. J. & Haslam, P. L. 1999 Damage to surfactant-specific protein in acute respiratory distress syndrome. *Lancet* **353** (9160), 1232–1237.

Bilek, A. M., Dee, K. C. & Gaver III, D. P. 2003 Mechanisms of surface-tension-induced epithelial cell damage in a model of pulmonary airway reopening. *J. Appl. Physiol.* **94** (2), 770–783.

Bretherton, F. P. 1961 The motion of long bubbles in tubes. *J. Fluid Mech.* **10** (2), 166–188.

Campana, D. M., Di Paolo, J. & Saita, F. A. 2004 A 2-D model of Rayleigh instability in capillary tubes: surfactant effects. *Intl J. Multiphase Flow* **30** (5), 431–454.

Cassidy, K. J., Halpern, D., Ressler, B. G., & Grotberg, J. B. 1999 Surfactant effects in model airway closure experiments. *J. Appl. Physiol.* **87** (1), 415–427.

Dargaville, P. A., South, M. & McDougall, P. N. 1996 Surfactant abnormalities in infants with severe viral bronchiolitis. *Arch. Dis. Child.* **75** (2), 133–136.

Everett, D. H. & Haynes, J. M. 1972 Model studies of capillary condensation. Part 1. Cylindrical pore model with zero contact angle. *J. Colloid Interface Sci.* **38** (1), 125–137.

Fairbrother, F. & Stubbs, A. E. 1935 Studies in electro-endosmosis. Part VI. The 'bubble-tube' method of measurement. *J. Chem. Soc.* **1**, 527–529.

Fujioka, H. & Grotberg, J. B. 2004 Steady propagation of a liquid plug in a two-dimensional channel. *J. Biomech. Engng Trans. Asme* **126** (5), 567–577.

Fujioka, H. & Grotberg, J. B. 2005 The steady propagation of a surfactant-laden liquid plug in a two-dimensional channel. *Phys. Fluids* **17** (8), 082102.

Fujioka, H., Takayama, S. & Grotberg, J. B. 2008 Unsteady propagation of a liquid plug in a liquid-lined straight tube. *Phys. Fluids* **20** (6), 062104.

Gauglitz, P. A. & Radke, C. J. 1988 An extended equation for liquid-film break up in cylindrical capillaries. *Chem. Engng Sci.* **43** (7), 1457–1465.

Ghadiali, S. N. & Gaver III, D. P. 2008 Biomechanics of liquid–epithelium interactions in pulmonary airways. *Respir. Physiol. Neurobiol.* **163** (1–3), 232–243.

Goerke, J. & Clements, J. A. 1986 *Alveolar Surface Tension and Lung Surfactant*. American Physiology Society.

Goldsmith, H. L. & Mason, S. G. 1963 Flow of suspensions through tubes. Part 2. Single large bubbles. *J. Colloid Sci.* **18** (3), 237–261.

Greaves, I. A., Hildebrandt, J. & Hoppin, J. F. G. 1986 *Handbook of Physiology. The Respiratory System. Mechanics of Breathing*. American Physiology Society.

Green, F. H. Y., Schurch, S., Desanctis, G. T., Wallace, J. A., Cheng, S. & Prior, M. 1991 Effects of hydrogen sulfide exposure on surface properties of lung surfactant. *J. Appl. Physiol.* **70** (5), 1943–1949.

Griese, M., Essl, R., Schmidt, R., Rietschel, E., Ratjen, F., Ballmann M. & Paul, K. 2004 Pulmonary surfactant, lung function, and endobronchial inflammation in cystic fibrosis. *Am. J. Respir. Crit. Care Med.* **170** (9), 1000–1005.

Guerin, C., LeMasson, S., DeVarax, R., MilicEmili, J. & Fournier, G. 1997 Small airway closure and positive end-expiratory pressure in mechanically ventilated patients with chronic obstructive pulmonary disease. *Am. J. Respir. Crit. Care Med.* **155** (6), 1949–1956.

Gunther, A., Siebert, C., Schmidt, R., Ziegler, S., Grimminger, F., Yabut, M., Temmesfeld, B., Walmrath, D., Morr, H. & Seeger, W. 1996 Surfactant alterations in severe pneumonia, acute respiratory distress syndrome, and cardiogenic lung edema. *Am. J. Respir. Crit. Care Med.* **153** (1), 176–184.

Halpern, D. & Gaver III, D. P. 1994 Boundary-element analysis of the time-dependent motion of a semi-infinite bubble in a channel. *J. Comput. Phys.* **115** (2), 366–375.

Halpern, D. & Grotberg, J. B. 1992 Fluid-elastic instabilities of liquid-lined flexible tubes. *J. Fluid Mech.* **244**, 615–632.

Halpern, D. & Grotberg, J. B. 1993 Surfactant effects on fluid-elastic instabilities of liquid-lined flexible tubes: a model of airway closure. *J. Biomech. Engng Trans. Asme* **115** (3), 271–277.

Halpern, D., Jensen, O. E. & Grotberg, J. B. 1998 A theoretical study of surfactant and liquid delivery into the lung. *J. Appl. Physiol.* **85** (1), 333–352.

Hammond, P. S. 1983 Nonlinear adjustment of a thin annular film of viscous-fluid surrounding a thread of another within a circular cylindrical pipe. *J. Fluid Mech.* **137**, 363–384.

Heil, M., Hazel, A. L. & Smith, J. A. 2008 The mechanics of airway closure. *Respir. Physiol. Neurobiol.* **163** (1–3), 214–221.

Hof, V. I., Gehr, P., Gerber, V., Lee, M. M. & Schurch, S. 1997 In vivo determination of surface tension in the horse trachea and in vitro model studies. *Respir. Physiol.* **109** (1), 81–93.

Huh, D., Fujioka, H., Tung,Y.-C., Futai, N., Paine, III, R., Grotberg, J. B. & Takayama, S. 2007 Acoustically detectable cellular-level lung injury induced by fluid mechanical stresses in microfluidic airway systems. *Proc. Natl Acad. Sci. USA* **104** (48), 18886–18891.

Kamm, R. D. & Schroter, R. C. 1989 Is airway closure caused by a liquid-film instability. *Respir. Physiol.* **75** (2), 141–156.

Kay, S. S., Bilek, A. M., Dee, K. C. & Gaver III, D. P. 2004 Pressure gradient, not exposure duration, determines the extent of epithelial cell damage in a model of pulmonary airway reopening. *J. Appl. Physiol.* **97** (1), 269–276.

Lee, M. M., Schurch, S., Roth, S . H., Jiang, X., Cheng, S., Bjarnason, S. & Green, F. H. 1995 Effects of acid aerosol exposure of the surface properties of airway mucus. *Exp. Lung Res.* **21** (6), 835–851.

Macklem, P. T., Proctor, D. F. & Hogg J. C. 1970 Stability of peripheral airways. *Respir. Physiol.* **8** (2), 191–203.

Muscedere, J. G., Mullen, J. B., Gan, K. & Slutsky, A. S. 1994 Tidal ventilation at low airway pressures can augment lung injury. *Am. J. Respir. Crit. Care Med.* **149** (5), 1327–1334.

Piirila, P. & Sovijarvi, A. R. A. 1995 Crackles: recording, analysis and clinical significance. *Eur. Respir. J.* **8** (12), 2139–2148.

Rayleigh, L. 1892 On the instability of cylindrical fluid surfaces. *Phil. Mag.* **34**, 177–180.

Reinelt, D. A. & Saffman, P. G. 1985 The penetration of a finger into a viscous fluid in a channel and tube. *Siam J. Sci. Stat. Comput.* **6** (3), 542–561.

Taskar, V., John, J., Evander, E., Robertson, B. & Jonson, B. 1997 Surfactant dysfunction makes lungs vulnerable to repetitive collapse and reexpansion. *Am. J. Respir. Crit. Care Med.* **155** (1), 313–320.

Taylor, G. I. 1961 Deposition of a viscous fluid on the wall of a tube. *J. Fluid Mech.* **10** (2), 161–165.

t Veen, J. C. C., Beekman, A. J., Bel, E. H. & Sterk, P. J. 2000 Recurrent exacerbations in severe asthma are associated with enhanced airway closure during stable episodes. *Am. J. Respir. Crit. Care Med.* **161** (6), 1902–1906.

Zheng, Y., Fujioka, H., Bian, S., Torisawa, Y., Huh, D., Takayama, S. & Grotberg, J. B. 2009 Liquid plug propagation in flexible microchannels: a small airway model. *Phys. Fluids* **21** (7), 071903.